Theoretical study of the photoionization of the excited $1s^2 2s2p\ ^{1,3}P^o$ states of the Be-like B^+ ion

Dae-Soung Kim*
e-Business Department, Kyonggi Institute of Technology, Siheung City, Jungwang-Dong 2121-3, Kyonggi-Do 429-792, Republic of Korea

Steven T. Manson
Department of Physics and Astronomy, Georgia State University, Atlanta, Georgia 30303, USA
(Received 20 August 2004; published 3 March 2005)

Photoionization of the first excited p states of the Be-like B^+ ion, which interact with the even-parity continua, has been studied theoretically. The calculated photoionization cross sections contain a number of autoionizing Rydberg series of resonances converging to the B^{2+} $2p$, $3s$, $3p$, and $3d$ states. Lower members of the Rydberg series of resonances with $n \leqslant 12$ are identified and resonance positions E_r, effective quantum numbers n^*, and widths Γ are presented. Excellent agreement between length- and velocity-gauge results is found, along with overall good agreement with previous work.

DOI: 10.1103/PhysRevA.71.032701 PACS number(s): 32.80.Fb

I. INTRODUCTION

The photoionization of the Be atom and Be-like ions offers an opportunity to study electron correlation in the simplest multishell atom and ions. Study of the ground-state photoionization reveals details of the odd-parity continua; excited p states, on the other hand, interact with the even-parity continua. In addition photoionization cross sections of Be and Be-like ions from both ground and excited states are needed for modeling of astrophysical and fusion plasmas. Total photoionization cross sections from the ground and several excited states including $2s2p\ ^{1,3}P^o$ states of Be and Be-like ions are reported by Tully *et al.* [1] as a part of the Opacity Project (OP). They calculated photoionization cross sections over a wide energy range using the OP R-matrix codes [2]. In addition, the investigation of photoionization in the energy range below the B^{2+} $2p$ threshold has been performed by Jannitti *et al.* [3] and Schippers *et al.* [4].

In the present work, we extend our previous photoionization calculations of the ground state of the Be-like B^+ ion [5] to the excited $2s2p\ ^{1,3}P$ states of the Be-like B^+ ion, and report the photoionization cross sections of these excited $2s2p\ ^{1,3}P^o$ states. For this detailed study of the partial and total cross sections, along with the doubly excited autoionizing levels from threshold up to the B^{2+} $3d$ threshold, we utilize the enhanced eigenchannel R-matrix approach [8,10,11]. The techniques applied here to describe excited-state photoionization are the same as those used previously for ground-state atomic Be [6,7]. A brief description of these techniques is given in the following section.

II. CALCULATION

In the present work, we considered the following photoionization processes:

$$B^+(2s2p\ ^{1,3}P^o) + \gamma \rightarrow [B^{2+}(ns) + \epsilon s]\ ^{1,3}S \tag{1}$$

$$\rightarrow [B^{2+}(ns) + \epsilon d]\ ^{1,3}D \tag{2}$$

$$\rightarrow [B^{2+}(np) + \epsilon p]\ ^{1,3}S,P,D \tag{3}$$

$$\rightarrow B^{2+}(np) + \epsilon f\ ^{1,3}D \tag{4}$$

where $n=2$ and 3 and γ represents the incident photon.

The major approximation in this calculational formalism concerns the use of a Hamiltonian H which does not refer to the full atomic system, but represents only the valence electrons plus an effective potential $U(r)$ to describe the e-B^{3+} interaction. We have adopted the following form of $U(r)$ [9]:

$$U(r) = -\frac{1}{r}[2 + (Z-2)e^{-\alpha_1 r} + \alpha_2 e^{-\alpha_3 r}] \tag{5}$$

where Z is the nuclear charge. The parameters α_i are chosen to optimize agreement between the calculated and experimental energy levels of the ground and valence excited states of B^+, and the values are 5.8571, 5.8524, and 6.2869.

The calculations employ a set of basis functions, y_i, which consists of all possible products of a set of one-electron orbitals outside the closed shell, as was done for the ground and excited states of atomic Be [6,7]. A superposition of these orthonormal basis functions is used in a small region inside the R-matrix volume of radius r_0 to obtain a variational estimate of the logarithmic derivative of the wave function at a given energy. We have used $r_0=10$ a.u. for the current calculations, a value that leads to excellent convegence. The calculation for coefficients c_i of the basis functions, $\psi_\beta = \Sigma_i\, c_i^\beta y_i$, is performed by a generalized configuration interaction (CI) approach based on the eigenchannel R-matrix method [11]. The basis set is divided into open and closed functions in this eigenchannel R-matrix approach, depending on their behavior over the reaction surface. The open functions are represented by the electron orbitals of the many-electron basis functions which are nonzero at the R-matrix boundary, while all of the electron orbitals represented by closed functions are zero at the boundary. We have

*Electronic address: dskim@kinst.ac.kr

TABLE I. Configuration for initial and final states in the photoionization of the Be-like B^+ $2s2p\ ^{1,3}P$ ion.

Initial state		Final state	
$nsmp$ ($npms$)	$^{1,3}P^o$	ns^2	^1S
$npmd$ ($ndmp$)		$nsmp$	$^{1,3}S$
$ndmf$ ($nfmd$)		$nsmd$($ndms$)	^1D
		np^2	^1S, ^3P, ^1D
		$npmp$	$^{1,3}S$,$^{1.3}P$, $^{1,3}D$
		$npmf$($nfmp$)	$^{1,3}D$
		nd^2	^1S, ^3P, ^1D
		$ndmd$	$^{1,3}S$,$^{1.3}P$, $^{1,3}D$
		nf^2	^1S, ^3P, ^1D
		$nfmf$	$^{1,3}S$,$^{1.3}P$, $^{1,3}D$

used two open orbitals and 20 closed orbitals for each l ($l \leqslant 5$). We include basis functions representing all possible symmetries resulting from the possible combinations of the one-electron orbitals as given in Table I, up to 10s, 11p, 12d, and 13f.

The calculated ionization energies leading to the ionic B^{2+} $2s\ ^2S$, $2p\ ^2P$, $3s\ ^2S$, $3p\ ^2P$, and $3d\ ^2D$ states relative to the excited $2p$ states of B^+ are given in Table II. For the ^3P initial state, the deviation of all thresholds from the NIST data [12] is no more than 23 meV. For the ^1P initial state the disagreement is as large as 95 meV: the separation among the thresholds agrees to within 20 meV, however. For the OP calculations [1], the thresholds are further off by at least an order of magnitude; the greatest deviation from the NIST data is more than 700 meV in the ^3P case and 800 meV for the ^1P case.

For the final state of the $B^{2+}+e^-$ system, a close-coupling expansion of all final channels arising from the $n=2$, 3, and 4 states of B^{2+} was included, with the exception of the $4f\epsilon h\ ^{1,3}D$ states; this omission should have no effect at all on our results, for two reasons. First is that the $l=5$ angular momentum barrier is so large that the dipole matrix element with this state will be vanishingly small at the energies considered herein. Second, the present photoionization calculation extends only to the B^{2+} $3d$ threshold so that the $4f$ channels will have only a tiny effect upon the cross sections near the $3d$ threshold and below.

The energy-normalized eigenstates ψ_α in each eigenchannel can be represented by a linear combination of the unnormalized eigenstates which, along with the ground-state wave function ψ_0, are used to calculate the reduced dipole matrix elements, given in length form as

$$d_\alpha(L) = \langle \psi_\alpha \| \vec{r}_1 + \vec{r}_2 \| \psi_0 \rangle. \quad (6)$$

The details of the above eigenchannel R-matrix formulation is discussed in detail elsewhere [13].

For the calculation of the resonance parameters, such as the resonance energies E_r, effective quantum numbers n^*, and widths Γ, we also have used the same ideas of eigenphase sum gradients as described in Ref. [14].

III. RESULTS AND DISCUSSION

A. Photoionization below the 2*p* threshold of B^{2+}

The photoionization cross sections for ionization to the B^{2+} $2s$ state from the excited $2s2p\ ^{1,3}P^o$ states are shown in Figs. 1(a) and 1(d), respectively, along with the associated partial cross sections in Figs. 1(b), 1(c), 1(e), and 1(f) for singlet and triplet cases, respectively. The length and velocity results, the solid and dotted curves, respectively, are displayed individually. The excellent agreement between the two indicates the accuracy of the calculation. The first, second, and third vertical dotted lines represent the B^{2+} $2p$, $3s$, and $3p$ ionization thresholds, respectively. As shown in Fig. 1, the features of photoionization spectra for each of the singlet and triplet processes differ in several aspects.

In the energy region below the B^{2+} $2p$ threshold, there are three Rydberg series for each of the triplet and singlet manifolds, each converging to the B^{2+} $2p$ threshold. The $^1P^o \rightarrow {}^1S^e$ cross section $\sigma_{2s\epsilon s}\ ^1S$, showing the $2pnp\ ^1S$ Rydberg series, is seen in Fig. 1(b); the $^1P^o \rightarrow {}^1D^e$ cross section $\sigma_{2s\epsilon d}\ ^1D$, showing the $2pnp\ ^1D$ and $2pnf\ ^1D$ Rydberg series, in Fig. 1(c). The analogous triplet cross sections, with the associated resonances, are presented in Figs. 1(e) and 1(f), respectively. The photoionization cross section leading to B^{2+} $2s$ from ^1P, shown in Fig. 1(a), is, of course, the sum of Figs. 1(b) and 1(c), while the cross section from $^3P^o$ shown in Fig. 1(d) is the sum of Figs. 1(e) and 1(f). Except for the resonances, the cross sections are seen to be dominated by the $p \rightarrow d$ channel ($2s\epsilon d$), in each case, by more than an order of magnitude, over the $p \rightarrow s$ ($2s\epsilon s$) channel. The reso-

TABLE II. Ionization thresholds (in eV) relative to the $2p$ excited states of atomic B^+.

State	$2s2p\ ^3P^o$ Calc.[a]	Calc.[b]	NIST[c]	$2s2p\ ^1P^o$ Calc.[a]	Calc.[b]	NIST[c]
$2s\ ^2S$	20.5217	19.8998	20.5239	15.9825	15.2842	16.0548
$2p\ ^2P^o$	26.5191	25.9582	26.5217	21.9799	21.3424	22.0526
$3s\ ^2S$	42.8427	42.1597	42.8661	38.3021	37.5441	38.3970
$3p\ ^2P^o$	44.4313	43.7559	44.4475	39.8922	39.1404	39.9784
$3d\ ^2D$	44.8317	44.1082	44.8335	40.2925	39.4926	40.3644

[a]Present result.
[b]OP data [1].
[c]NIST data [12].

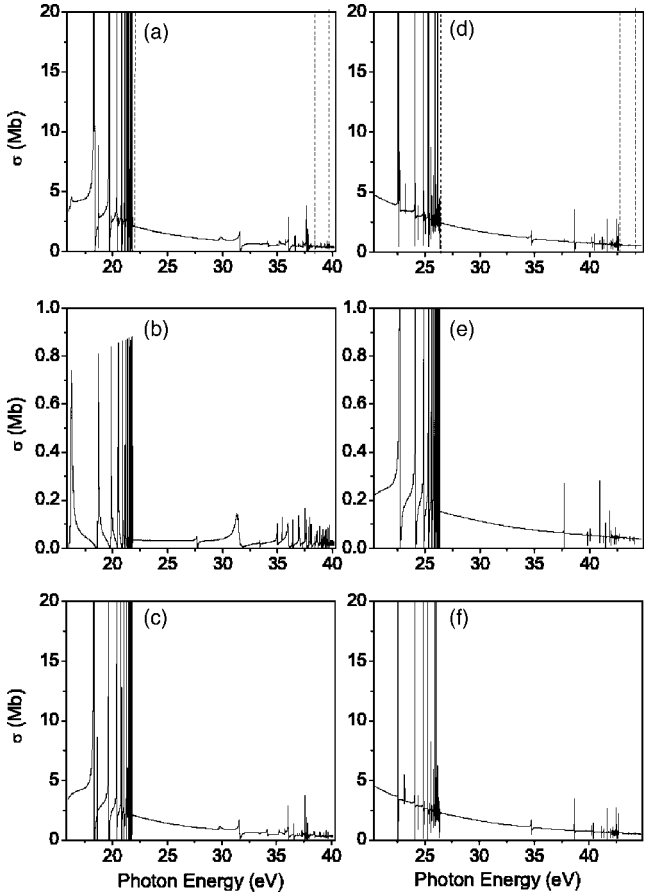

FIG. 1. (a) Photoionization cross sections leading to the B^{2+} $2s$ state from the excited $2s2p\ ^1P^o$ states as a function of photon energy; (b) $\sigma_{2s\epsilon s\ ^1S}$; (c) $\sigma_{2s\epsilon d\ ^1D}$. (d) Photoionization cross sections leading to the B^{2+} $2s$ state from the excited $2s2p\ ^3P^o$ states as a function of photon energy; (e) $\sigma_{2s\epsilon s\ ^3S}$; (f) $\sigma_{2s\epsilon d\ ^3D}$. Solid curve, present length results; dotted curve, present velocity results. The vertical dotted lines represent the B^+ $2p$, $3s$, and $3p$ thresholds, respectively.

nances have been studied in detail and their energy positions E_r, effective quantum numbers n^*, and widths Γ are given in Table III.

The photoionization of the excited $2s2p\ ^{1,3}P^o$ states of B^+ differs from the case of atomic Be [7] in that the $2p^2\ ^1S$, ^1D, $2p3p\ ^3S$, and $2p3p\ ^{1,3}D$ are true bound states in B^+, i.e., they lie below the B^{2+} $2s$ threshold, as seen in Fig. 1 and Table III. It is also seen that the $2pnp$ singlet resonances are significantly wider than the triplet resonances, the same as in the atomic Be case. This is because the singlet resonances are spatially symmetric so the two electrons are, on the averqge, closer together than in the triplet counterpart; being closer together, they interact more strongly, thereby increasing the width. However, unlike Be, the D resonances are narrower than the corresponding S resonances for both singlet and triplet cases. Other differences involve the line profiles. In the Be cases, the $2pnp\ ^1D$, ^1S, and ^3S series all show positive q values, while for the $2pnp\ ^3D$ series, q is negative. However, for B^+, the $2pnp\ ^1D$, ^3D, and ^3S series all exhibit positive q values, while for $2pnp\ ^1S$, q is negative. Since the singlet resonances are so much wider than the triplet, the ^1P cross section below the $2p$ threshold is seen to be completely dominated by the resonances. This contrasts with the ^3P case where the very narrow resonances appear on a monotonically decreasing background cross section. In addition, as mentioned above, the $2p3p\ ^3P$ state is a true bound state, but the $2p3p\ ^1P$ lies just above threshold, as seen in Fig. 1(a) and Table III. This near-threshold resonance in the ^1P case results in a further difference between singlet and triplet cross sections.

The $2pnf\ ^{1,3}D$ series are very weak in both the singlet and triplet cases. They are also very narrow resonances with the singlet series being much narrower, by about an order of magnitude, than the triplets; just the opposite of the $2pnp$ series where the singlets were significantly wider than the triplets. Clearly, correlation plays an important role in the widths of the $2pnf\ ^{1,3}D$ resonances that alters the phenomenology from the intuitive notion.

It is clear from Table III that all of these series display smooth regular behavior with approximately constant quantum defects. For the various $2pnp$ series, the largest quantum defect (lowest energy) is seen to occur for the ^3D series with a value of about 0.29, with the least bound being the ^1S series which has a quantum defect of about -0.04, indicating that exchange is strongly repusive for the ^1S states. The $2pnf$ series both have a slightly negative quantum defect of about -0.03, consistent with the fact that nf states are nearly hydrogenic for such low Z.

B. Photoionization between the B^{2+} $2p$ and $3s$ thresholds

In the energy range between the B^{2+} $2p$ and $3s$ thresholds, the photoionization process can leave the B^{2+} ion in either the ground $2s$ state or the first excited $2p$ state. More specifically, along with the $2s\epsilon s\ ^{1,3}S^e$ and $2s\epsilon d\ ^{1,3}D^e$ channels that were already open, the $2p\epsilon p\ ^{1,3}S^e$, P^e, D^e and $2p\epsilon f\ ^{1,3}D^e$ channels open above the B^{2+} $2p$ threshold. Thus, the $^{1,3}S$ and $^{1,3}D$ manifolds of final continuum states can branch to either B^{2+} $2s$ or B^{2+} $2p$ channels, but the $^{1,3}P$ manifold can lead only to the B^{2+} $2p$ channel.

The photoionization cross sections leading to the B^{2+} $2p$ state from the excited $2s2p\ ^{1,3}P^o$ states are shown in Figs. 2(a) and 2(f), respectively. The partial cross sections $\sigma_{2p\epsilon p}\ ^1S$, ^1P, ^1D and $\sigma_{2p\epsilon f}\ ^1D$ for singlet processes are shown in Figs. 2(b)–2(e), while corresponding cross sections for triplet cases are shown in Figs. 2(g)–2(j).

As shown in Fig. 1 for B^{2+} $2s$ production, both the singlet and triplet cross sections are dominated by the $p \rightarrow d$ $(2s\epsilon d)$ channels, more than an order of magnitude over the $p \rightarrow s$ $(2s\epsilon s)$ channel. In addition, the background cross sections are of roughly the same size in both singlet and triplet cases. For B^{2+} $2p$ production, the background cross section is significantly larger for the singlet initial state as compared to the triplet, as seen in Fig. 2. The dominant contribution to the singlet cross section is seen to be the $2p\epsilon p\ ^1D$ channel; the cross section for the corresponding ^3D channel is much smaller, and this is the primary reason that the singlet cross section is so much larger than the triplet for B^{2+} $2p$ production.

In addition, as seen in Fig. 2, the resonance patterns are significantly more complicated in the region between the B^{2+}

TABLE III. Resonance position (E_r in eV), effective quantum numbers (n^*), and widths (Γ in eV) of autoionizing levels converging to the B^{2+} $2p$ threshold.

	$2pnp\ ^1S$			$2pnp\ ^3S$				
				Present	Ref. [3]	Ref. [4]		
n	E_r	n^*	Γ	E_r	E_r	E_r	n^*	Γ
3	16.2162	3.0729	0.1468					
4	18.6764	4.0589	0.0749	22.7166	22.77	22.806	3.7832	0.0252
5	19.8478	5.0523	0.0421	24.1419	24.06	24.102	4.7847	0.0205
6	20.4923	6.0485	0.0256	24.8939		24.879	5.7868	0.0129
7	20.8838	7.0464	0.0165	25.3382		25.352	6.7886	0.0083
8	21.1391	8.0452	0.0113	25.6221		25.637	7.7894	0.0056
9	21.3146	9.0445	0.0081	25.8146		25.831	8.7895	0.0039
10	21.4404	10.0432	0.0059	25.9513		25.963	9.7901	0.0028
11	21.5337	11.0439	0.0045	26.0517		26.064	10.7909	0.0021
12	21.6047	12.0439	0.0035	26.1277		26.144	11.7916	0.0017
	$2pnp\ ^1D$			$2pnp\ ^3D$				
				Present	Ref. [3]	Ref. [4]		
n	E_r	n^*	Γ	E_r	E_r	E_r	n^*	Γ
4	18.3040	3.8478	0.0156	22.5967		22.607	3.7149	0.0119
5	19.6644	4.8481	0.0054	24.0979	24.06	24.102	4.7179	0.0029
6	20.3885	5.8479	0.0027	24.8793	24.87	24.879	5.7198	0.0011
7	20.8194	6.8480	0.0017	25.3377		25.352	6.7184	0.0005
8	21.0962	7.8477	0.0005	25.6295		25.637	7.7169	
9	21.2848	8.8483	0.0004	25.8266		25.831	8.7154	
10	21.4182	9.8436	0.0004	25.9659		25.963	9.7148	
11	21.5170	10.8433	0.0003	26.0683		26.064	10.7123	
12	21.5919	11.8437	<0.0001	26.1453		26.144	11.7113	
	$2pnf\ ^1D$			$2pnf\ ^3D$				
n	E_r	n^*	Γ	E_r			n^*	Γ
4	18.6370	4.0349	0.0003	23.1694			4.0294	0.0029
5	19.8317	5.0343	<0.0001	24.3873			5.0374	0.0023
6	20.4852	6.0341		25.0429			6.0359	0.0013
7	20.8801	7.0347		25.4203			7.0334	
8	21.1368	8.0343		25.6781			8.0327	
9	21.3131	9.0346		25.8541			9.0321	
10	21.4393	10.0341		25.9808			10.0320	
11	21.5246	11.0344		26.0746			11.0321	
12	21.6043	12.0346		26.1455			12.0319	

$2p$ and $3s$ thresholds than below the B^{2+} $2p$ threshold. This occurs because, although there are only two series of resonances converging to the B^{2+} $3s$ threshold for each of the initial states, the B^{2+} $n=3$ thresholds are so close in energy that the lower members of resonant series converging to B^{2+} $3p$ and $3d$ thresholds lie below the $3s$ threshold. These interlopers interact strongly with the resonances converging to the B^{2+} $3s$ threshold, resulting in alterations of resonance positions, widths, shapes, and strengths of all of the interacting resonances.

Analysis of the resonances arising from both the singlet and triplet initial states converging to the B^{2+} $3s$ threshold, shown in Table IV, clearly indicates the presence of interlopers from resonance series converging to other thresholds by the sudden changes in quantum defect, and anomalies in width, in going along a given series.

In the ^1S case the lowest resonance, at 27.700 eV and identified as $3s^2\ ^1S$, is seen as a weak structure in the B^{2+} $2p$ channel, Figs. 2(a) and 2(b), and the B^{2+} $2s$ channel, Fig. 1(b). The branching to the two possible decay channels is seen to be about the same, but the shapes are quite different; close to a symmetric Lorentzian for the B^{2+} $2p$ channel, but a completely asymmetric Fano profile in the B^{2+} $2s$ channel. Note also that this resonance is absent in the OP result [1].

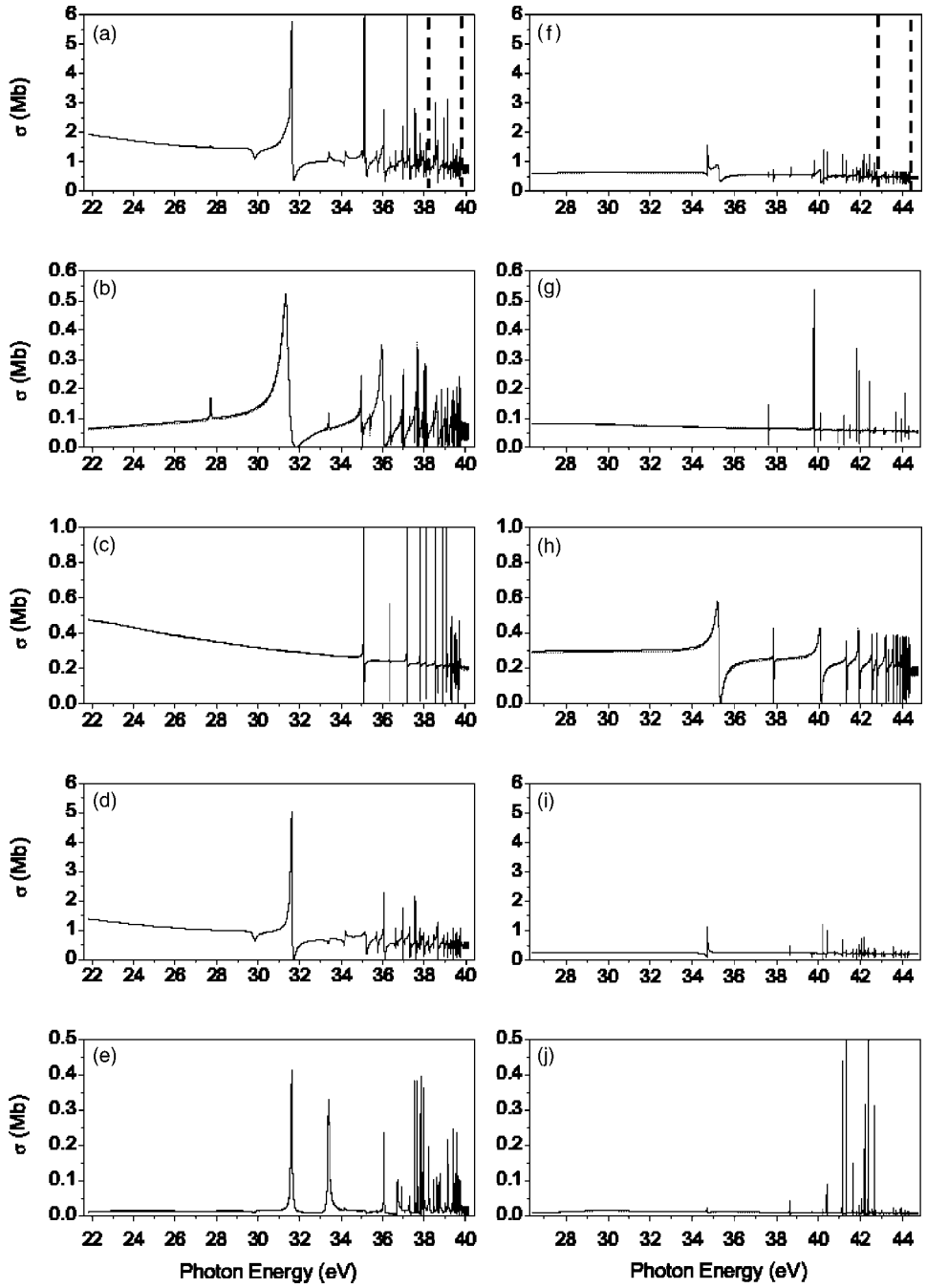

FIG. 2. (a) Photoionization cross sections leading to the B^{2+} $2P$ state from the excited $2s2p\ ^1P^o$ states as a function of photon energy; (b) $\sigma_{2p\epsilon p\ ^1S}$; (c) $\sigma_{2p\epsilon p\ ^1P}$. (d) $\sigma_{2p\epsilon p\ ^1D}$; (e) $\sigma_{2p\epsilon f\ ^1D}$. (f) Photoionization cross sections leading to the B^{2+} $2p$ state from the excited $2s2p\ ^3P^o$ states as a function of photon energy; (g) $\sigma_{2p\epsilon p\ ^3S}$; (h) $\sigma_{2p\epsilon p\ ^3P}$; (i) $\sigma_{2p\epsilon p\ ^3D}$; (j) $\sigma_{2p\epsilon f\ ^3D}$. Solid curve, present length results; dotted curve, present velocity results. The vertical dotted lines represent the B^+ $3s$, and $3p$ thresholds, respectively.

The next ^1S resonance, at 31.519 eV, is $3p^2\ ^1S$, an interloper that converges to the B^{2+} $3p$ threshold, as shown in Table V. This is a strong, broad resonance in both decay channels. The $3d^2\ ^1S$ at 35.004 eV is the next interloper, but it converges to the B^{2+} $3d$ threshold, as seen from Table VI. From the tables, it is seen that the $3pnp\ ^1S$ resonances for n up to 6 lie below the B^{2+} $3s$ threshold, as do the $3dnd\ ^1S$ for n up to 5, a total of seven interlopers in the ^1S manifold of resonances. As a consequence, the $3sns\ ^1S$ resonances are strongly perturbed and follow no regular pattern along the series, as seen in Table IV.

The ^1D resonances are seen to follow the same general pattern with one added complication; there are both the $2p\epsilon p\ ^1D$ and the $2p\epsilon f\ ^1D$ final states leading to the B^{2+} $2p$ channel. The former is reached by a one-electron transition from the initial state, but the latter is forbidden without correlation. Thus, the $2p\epsilon p\ ^1D$ cross section should be much larger than the $2p\epsilon f\ ^1D$, and this is indeed the case by about an order of magnitude, as seen in Figs. 2(d) and 2(e).

In the $2p\epsilon p\ ^1D$ cross section, the lowest ^1D resonance is the $3s3d\ ^1D$ at 29.811 eV which is seen to be quite weak. Its manifestation is quite different in the two decay channels, showing up as a window resonance in the B^{2+} $2p$ channel. The next resonance is an interloper converging to the B^{2+} $3p$ threshold, the $3p^2\ ^1D$ at 31.614 eV (Table V), which is strong and branches predominantly to the B^{2+} $2p$ channel, as seen in Figs. 1(c) and 2(d). As for the interlopers converging to the B^{2+} $3d$ threshold, the $3d^2\ ^1D$ at 33.396 eV is seen to

TABLE IV. Resonance positions (E_r in eV), effective quantum numbers (n^*), and widths (Γ in eV) of autoiononizing levels converging of the B^{2+} 3*s* threshold.

	$3sns\ ^1S$			$3sns\ ^3S$		
n	E_r	n^*	Γ	E_r	n^*	Γ
3	27.7125	2.2670	0.0529			
4	33.4012	3.3324	0.0257	37.6224	3.2288	0.0008
5	35.4138	4.3408	0.0095	39.7668	4.2063	0.0011
6	36.4139	5.3687	0.0104	40.8982	5.2904	0.0005
7	37.0252	6.5285	0.0376	41.4602	6.2742	0.0004
8	37.2945	7.3492	0.0018	41.7969	7.2139	0.0004
9	37.5170	8.3260	0.0018	42.0613	8.3456	0.0004
10	37.6961	9.4764	0.0169	42.2147	9.3094	0.0004
11	37.7954	10.3642	0.0014	42.3290	10.2933	0.0003
12	37.8792	11.3447	0.0008	42.4153	11.2848	<0.0001
	$3snd\ ^1D$			$3snd\ ^3D$		
n	E_r	n^*	Γ	E_r	n^*	Γ
3	29.8111	2.5317	0.2299	34.7283	2.5927	0.0281
4	33.8532	3.4975	<0.0001	38.6581	3.6141	0.0031
5	35.7453	4.6137	0.0256	40.3935	4.7313	0.0017
6	36.5975	5.6505	0.0095	41.1374	5.6793	0.0012
7	37.0925	6.7077	0.0094	41.6246	6.7341	0.0009
8	37.3109	7.4101	0.0308	41.9545	7.9083	0.0012
9	37.5559	8.5404	0.0034	42.1389	8.9088	0.0013
10	37.7222	9.6874	0.0053	42.2446	9.6861	0.0014
11	37.8142	10.5617	0.0046	42.3023	10.2069	0.0010
12	37.9149	11.8565	0.0042	42.3966	11.2748	0.0006

be quite weak, but the $3d4d\ ^1D$ resonance at 36.073 eV is seen quite strong. This shows that when interlopers interact with a Rydberg series, the interaction significantly modifies not only the Rydberg series, but the interlopers as well. The ^1D series is further complicated by interactions with interlopers from the $3pnf\ ^1D$ (Table V) and the $3dns\ ^1D$ (Table VI) series, thereby leading to the complexity seen.

In the $2p\epsilon f\ ^1D$ cross section, the background cross section is quite small [Fig. 2(e)] and the decay of the $3snd\ ^1D$ resonances to the $2p\epsilon f\ ^1D$ is extemely weak. Thus, the $2p\epsilon f\ ^1D$ cross section is completely dominated by the interlopers.

The ^1P resonances are completely different from the ^1S or the ^1D. There are no ^1P resonances converging to B^{2+} 3*s* and they can decay solely to the B^{2+} 2*p* channel. Thus, the ^1P resonances in this region are the lower members of series converging to B^{2+} 3*p* and 3*d* thresholds. Even though there is no underlying Rydberg series to interact with, the $3pnp\ ^1P$ and the $3dnd\ ^1P$ series perturb each other. Since there are only a small number of resonances in this energy region, the cross section is very much simpler than the others, as seen in Fig. 2(c).

The ^3S and ^3D resonances in the $2s2p\ ^3P^o$ cross section show phenomenology generally similar to their singlet counterparts, but they are missing the very strong $3l^2$ resonances which have no ^3S or ^3D multiplets. Thus the resonances are less important in these cases. On the other hand, for the ^3P, the strong $3l^2$, which are absent in the ^1P manifold, have considerable influence, making the resonances more important in the ^3P case, as seen in Fig. 2(h).

The widths of the ^1S and ^1D singlet resonances are seen in Table IV and Fig. 2 to be about an order of magnitude larger than their triplet counterparts; and this occurs partially for the same reason as the lower resonances discussed in the section, along with the perturbation of the strong $3l^2$ interlopers. The ^3P resonances, on the other hand, are wider than their singlet counterparts, owing to the perturbation of the $3l^2$ resonances.

C. Photoionization between the B^{2+} 3*s* and 3*p* thresholds

Above the B^{2+} 3s threshold, the channels leading to the B^{2+} $3s\ ^2S$ state open, in addition to the channels already open. The photoionization cross sections for B^{2+} 3*s* production between the B^{2+} 3*s* and 3*p* thresholds from each of the singlet and triplet initial states are shown in Figs. 3(a) and 3(d), respectively, while the related partial channel cross sections are shown in Figs. 3(b), 3(c), 3(e), and 3(f), respectively; the B^{2+} 2*s* and 2*p* production cross sections in this region are shown in Figs. 1 and 2, respectively.

The B^{2+} 3*s* production cross sections are fundamentally different from the two lower B^{2+} cross sections in one very important way: Photoionization to the B^{2+} $2s\ ^2S$ or B^{2+}

TABLE V. Resonance positions (E_r in eV), effective quantum numbers (n^*), and widths (Γ in eV) of autoionizing levels converging of the B^{2+} $3p$ threshold.

	$3pnp\ ^1S$			$3pnp\ ^3S$		
n	E_r	n^*	Γ	E_r	n^*	Γ
3	31.4209	2.5346	0.3662			
4	36.0083	3.7433	0.1449	40.0449	3.5224	0.0019
5	37.6589	4.9366	0.0181	42.0626	4.7933	0.0746
6	38.2026	5.6755	0.0009	42.7675	5.7194	0.0403
7	38.6429	6.6002	0.0599	43.2702	6.8462	0.0155
8	38.8636	7.2738	0.0064	43.4961	7.6283	0.0193
9	39.1306	8.4532	0.0219	43.7244	8.7743	0.0121
10	39.2505	9.2093	0.0019	43.8431	9.6186	0.0097
11	39.3976	10.4898	0.0142	43.9669	10.8263	0.0058
12	39.4648	11.2839	0.0046	44.0328	11.6862	
	$3pnp\ ^1P$			$3pnp\ ^3P$		
n	E_r	n^*	Γ	E_r	n^*	Γ
3				35.2492	2.4346	0.1544
4	35.1099	3.3734	0.0019	40.0594	3.5282	0.0768
5	37.1862	4.4846	0.0006	41.8821	4.6205	0.0243
6	38.1053	5.5188	0.0005	42.7366	5.6668	0.0067
7	38.6588	6.6426	<0.0001	43.1535	6.5263	0.0128
8	38.9217	7.4886	0.0006	43.4885	7.5978	0.0058
9	39.1468	8.5449	0.0013	43.6592	8.3955	0.0053
10	39.2866	9.4795	0.0005	43.8393	9.5879	0.0029
11	39.4044	10.5625	<0.0001	43.9327	10.4474	0.0033
12	39.4795	11.4838	<0.0001	44.0281	11.6175	0.0009
	$3pnp\ ^1D$			$3pnp\ ^3D$		
n	E_r	n^*	Γ	E_r	n^*	Γ
3	31.6138	2.5640	0.0732			
4	34.1641	3.0821	0.0433	39.7011	3.3919	0.0064
5	36.9293	4.2858	0.0038	41.6246	4.4035	0.0009
6	37.9655	5.3147	0.0020	42.6103	5.4668	0.0056
7	38.6306	6.5681	0.0035	43.1385	6.4882	0.0018
8	38.8268	7.1471	0.0361	43.4822	7.5726	0.0140
9	39.0688	8.1297	0.0208	43.6379	8.2819	0.0008
10	39.2383	9.1226	0.0186	43.8426	9.6152	0.0058
11	39.3598	10.1102	0.0112	43.9337	10.4576	0.0008
12	39.4514	11.1120	0.0105	43.9991	11.2211	0.0052
	$3pnf\ ^1D$			$3pnf\ ^3D$		
n	E_r	n^*	Γ	E_r	n^*	Γ
4	36.7113	4.1364	0.0460	40.7876	3.8647	0.0015
5	37.6308	4.9057	0.0025	42.2438	4.9879	0.0009
6	38.4532	6.1497	0.0139	42.9203	6.0015	0.0392
7	38.7564	6.9222	0.0178	43.3278	7.0229	0.0229
8	39.0069	7.8407	0.0165	43.5850	8.0194	0.0005
9	39.1876	8.7887	0.0102	43.7179	8.7342	0.0087
10	39.3278	9.8196	0.0090	43.8723	9.8670	0.0011
11	39.4317	10.8714	0.0062	43.9719	10.8838	0.0044
12	39.4904	11.6375	0.0060	44.0449	11.8692	0.0038

TABLE VI. Resonance positions (E_r in eV), effective quantum numbers (n^*), and widths (Γ in eV) of autoionizing levels converging to the B^{2+} $3d$ threshold.

	$3dnd\ ^1S$			$3dnd\ ^3S$		
n	E_r	n^*	Γ	E_r	n^*	Γ
3	35.0047	3.2082	0.0369			
4	37.0253	4.0813	0.0376	41.1833	3.8623	0.0012
5	38.0721	4.9508	0.0035	42.4015	4.7322	0.0018
6	38.4441	5.4262	0.0083	43.1113	5.6244	0.0105
7	39.0293	6.5638	0.0242	43.6265	6.7198	0.0011
8	39.3401	7.5591	0.0155	43.9162	7.7101	0.0021
9	39.5602	8.6206	0.0124	44.1193	8.7409	0.0039
10	39.7041	9.6172	0.0032	44.2652	9.7909	0.0006
11	39.8091	10.6103	0.0359	44.3599	10.7399	0.0157
12	39.8890	11.6141	0.0301	44.4367	11.7375	0.0119
	$3dnd\ ^1P$			$3dnd\ ^3P$		
n	E_r	n^*	Γ	E_r	n^*	Γ
3				37.8444	2.7909	0.0018
4	36.3525	3.7166	0.0024	41.3036	3.9275	0.0084
5	37.8124	4.6844	0.0011	42.5241	4.8564	0.0131
6	38.5628	5.6093	0.0019	43.2824	5.9269	0.0007
7	39.0769	6.6909	0.0010	43.7167	6.9865	0.0020
8	39.4044	7.8282	<0.0001	43.9666	7.9315	<0.0001
9	39.5947	8.8310	<0.0001	44.1475	8.9185	<0.0001
10	39.7465	9.9840	<0.0001	44.2783	9.9170	<0.0001
11	39.8260	10.8008	0.0008	44.3709	10.8681	0.0081
12	39.8941	11.6875	0.0043	44.4454	11.8698	0.0062
	$3dnd\ ^1D$			$3dnd\ ^3D$		
n	E_r	n^*	Γ	E_r	n^*	Γ
3	33.3945	2.8089	0.0968			
4	36.0728	3.5913	0.0231	41.3142	3.9334	0.0013
5	37.7224	4.6017	0.0059	42.6404	4.9835	<0.0001
6	38.6359	5.7318	0.0173	43.3278	6.0157	0.0229
7	39.1209	6.8158	0.0098	43.7179	6.9912	0.0087
8	39.3960	7.7915	0.0055	43.9719	7.9557	0.0044
9	39.5911	8.8086	0.0044	44.1608	9.0065	0.0022
10	39.7259	9.8009	0.0017	44.2851	9.9784	0.0020
11	39.8293	10.8398	0.0132	44.3789	10.9641	0.0046
12	39.9040	11.8350	0.0101	44.4517	11.9674	0.0028
	$3dns\ ^1D$			$3dns\ ^3D$		
n	E_r	n^*	Γ	E_r	n^*	Γ
4	35.2072	3.2714	0.0772	40.3935	3.5018	0.0017
5	37.3712	4.3162	0.0050	42.3023	4.6386	0.0025
6	38.2314	5.1386	0.0247	43.1385	5.6694	0.0018
7	38.9286	6.3168	0.0076	43.5924	6.6267	0.0131
8	39.2836	7.3444	0.0042	43.9032	7.6559	0.0064
9	39.5149	8.3657	0.0033	44.1096	8.6814	0.0018
10	39.6668	9.3261	0.0049	44.2396	9.5873	0.0009
11	39.7814	10.3187	0.0023	44.3570	10.7077	0.0023
12	39.8741	11.4051	0.0095	44.4346	11.7074	0.0032

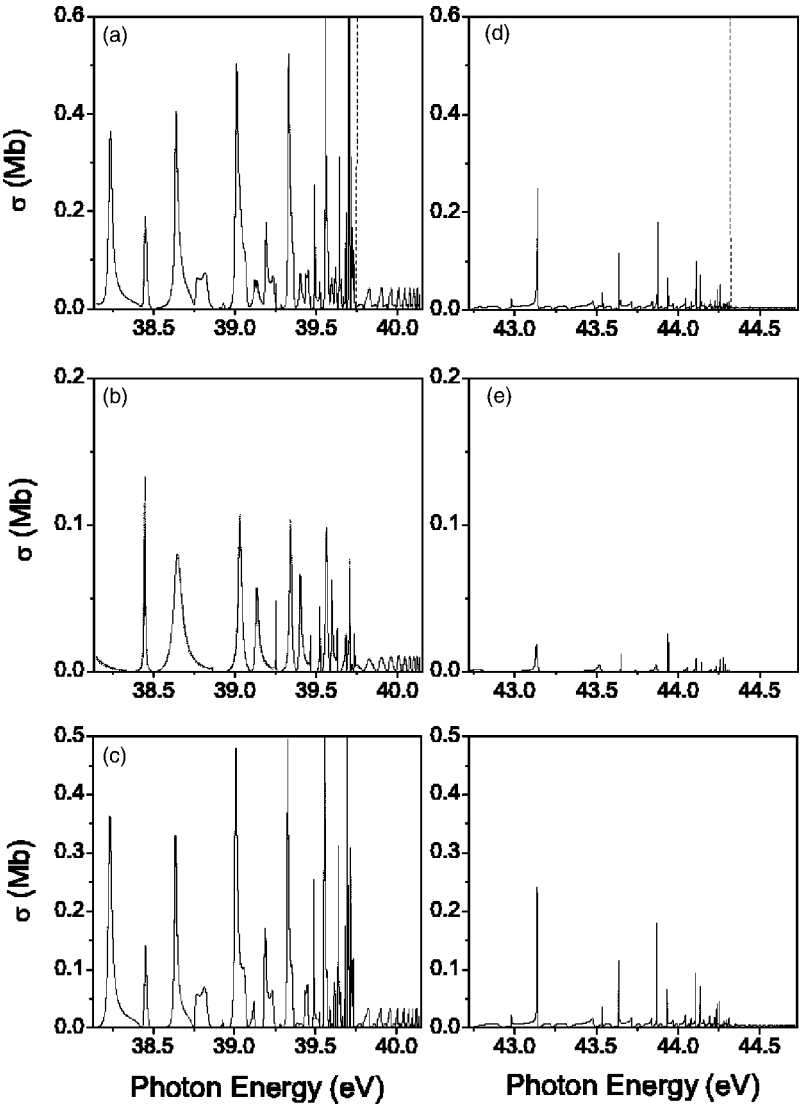

FIG. 3. (a) Photoionization cross sections leading to the B^{2+} 3*s* state from the excited $2s2p\ ^1P^o$ states as a function of photon energy; (b) $\sigma_{3s\epsilon s\ ^1S}$; (c) $\sigma_{3s\epsilon d\ ^1D}$. (d) Photoionization cross sections leading to the B^{2+} 3*s* state from the excited $2s2p\ ^3P^o$ states as a function of photon energy; (e) $\sigma_{3s\epsilon s\ ^3S}$; (f) $\sigma_{3s\epsilon d\ ^3D}$. Solid curve, present length results; dotted curve, present velocity results. The vertical dotted lines represent the B^{2+} 3*p* threshold.

$2p\ ^2P$ are primarily single-electron transitions, predominantly $2p \rightarrow \epsilon s, d$ or $2s \rightarrow \epsilon p$, respectively. Photoionization to the B^{2+} $3s\ ^2S$ state, on the other hand, requires a two-electron transition, i.e., photoionization plus excitation. This two-electron process is much less likely than a single-electron transition; consequently, it is expected that the background (nonresonant) cross section in this channel will be extremely small. From Fig. 3, it is evident that this is indeed the case. On the scales shown, the nonresonant continuum cross sections are too small to appear. Thus, the strength of the B^{2+} 3*s* cross sections, from both singlet and triplet states, is almost entirely due to resonances in the newly opened B^+ 3*s* channels.

The resonance structure in this region gets even more complex owing to the very small energy difference ~0.4 eV between the 3*p* and 3*d* thresholds of B^{2+}. This is evident from Table V where the details of the four resonant singlet and four resonant triplet series converging on the B^{2+} 3*p* state are given and quite a number of anomalies are seen in the quantum defects and widths in virtually every series owing to interlopers from the lower (and not so low) members of series converging on B^{2+} 3*d*. As was the case previously, the singlet series are wider than the triplets, with one exception. As dicussed above, because of the series perturbations caused by interlopers, the members of the $3pnp\ ^3P$ are wider than the corresponding ^1P resonances; this is abundantly clear from Figs. 2(c) and 2(h) and Table V.

D. Photoionization between the B^{2+} 3*p* and 3*d* thresholds

In this energy region, the B^{2+} 3*p* channel opens, in addition to the lower channels already open. The cross sections for photoionization leading the production of B^{2+} 3*p* from both singlet and triplet initial states are shown in Fig. 4. It is evident from the figure that for both singlet and triplet cases, the background (nonresonant) cross sections are tiny, too small to appear on the scale of the figure. In the total B^{2+} 3*p* cross section, in each case, there appears to be a background, but closer scrutiny reveals that this apparent background is simply the sum of the various resonant series, Figs. 4(b)–4(e) for the singlet case and Figs. 4(g)–4(j) for the triplet. The smallness of the background cross sections occurs for exactly the same reason as discussed in the previous section for the B^{2+} 3*s* cross sections; these channels represent two-electron

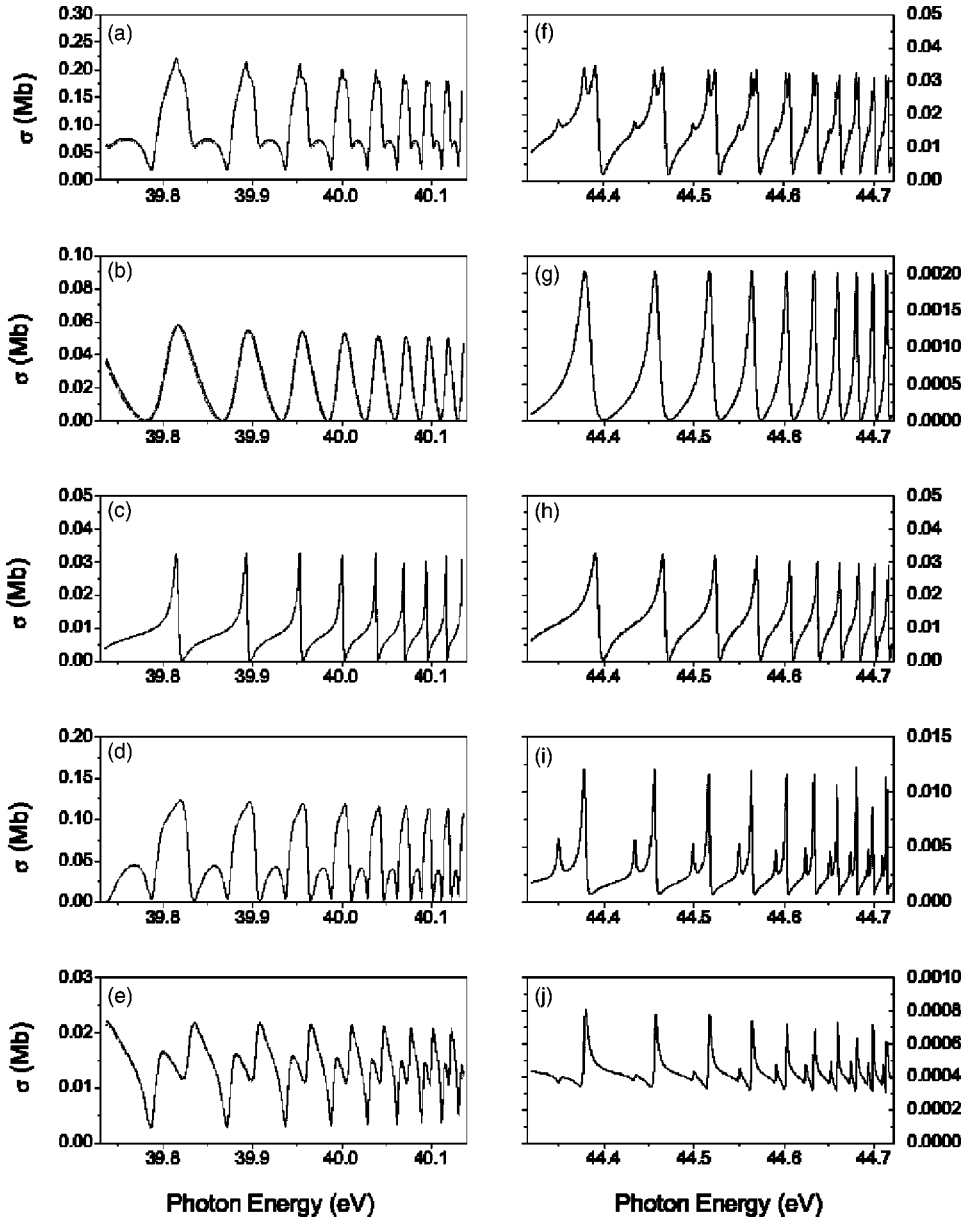

FIG. 4. (a) Photoionization cross sections leading to the B^{2+} $3p$ state from the excited $2s2p\ ^1P^o$ states as a function of photon energy; (b) $\sigma_{3p\epsilon p\ ^1S}$; (c) $\sigma_{3p\epsilon p\ ^1P}$; (d) $\sigma_{3p\epsilon p\ ^1D}$; (e) $\sigma_{3p\epsilon f\ ^1D}$. (f) Photoionization cross sections leading to the B^{2+} $3p$ state from the excited $2s2p\ ^3P^o$ states as a function of photon energy; (g) $\sigma_{3p\epsilon p\ ^3S}$; (h) $\sigma_{3p\epsilon p\ ^3P}$; (i) $\sigma_{3p\epsilon p\ ^3D}$; (j) $\sigma_{3p\epsilon f\ ^3D}$. Solid curve, present length results; dotted curve, present velocity results.

ionization plus excitation processes. There are four series of resonances leading up to the B^{2+} $3d$ threshold in the singlet case, $3dnd\ ^1S$, ^1P, ^1D and $3dns\ ^1D$, along with the corresponding four series in the triplet case. The details of the resonant series are given in Table VI. Many of the lower members of each of the series lie below the B^{2+} $3p$ and a few even below the B^{2+} $3s$; this is a consequence of the fact that the $n=3$ thresholds are so close together in energy.

Owing to the overlapping of the various series of resonances converging on B^{2+} $3d$ with the series converging to the two lower thresholds of B^{2+}, there is no regularity in the parameters of the lower members of the various series of resonances detailed in Table VI. However, for the parts of the series that lie above the B^{2+} $3p$ threshold, there are no more overlapping series converging to different limits; the lowest members of the next resonance series, those converging to B^{2+} $4s$, are higher in energy. Thus, it is expected that above the B^{2+} $3p$ threshold, the parameters of the series converging to B^{2+} $3d$ will behave smoothly. This is exactly what is observed in Table VI.

In addition, the resonances in all channels are seen to be quite weak, so the background (nonresonant) cross section in the single-electron-excitation channels leading to the $2s$ and $2p$ state of B^{2+} dominate.

E. Total photoionization cross sections

The total photoionization cross sections for the photoionization of the excited $2s2p\ ^{1,3}P^o$ states of ionic B^+ are obtained by adding respective partial cross sections. The present and OP results [1] for the total photoionization cross sections of the excited $2s2p\ ^{1,3}P^o$ states are shown in Fig. 5. Our results show rather good overall agreement with the OP results. However, there are significant discrepancies between the two different results for both singlet and triplet cases. First, OP results for cross sections at the B^{2+} $2s$ threshold are

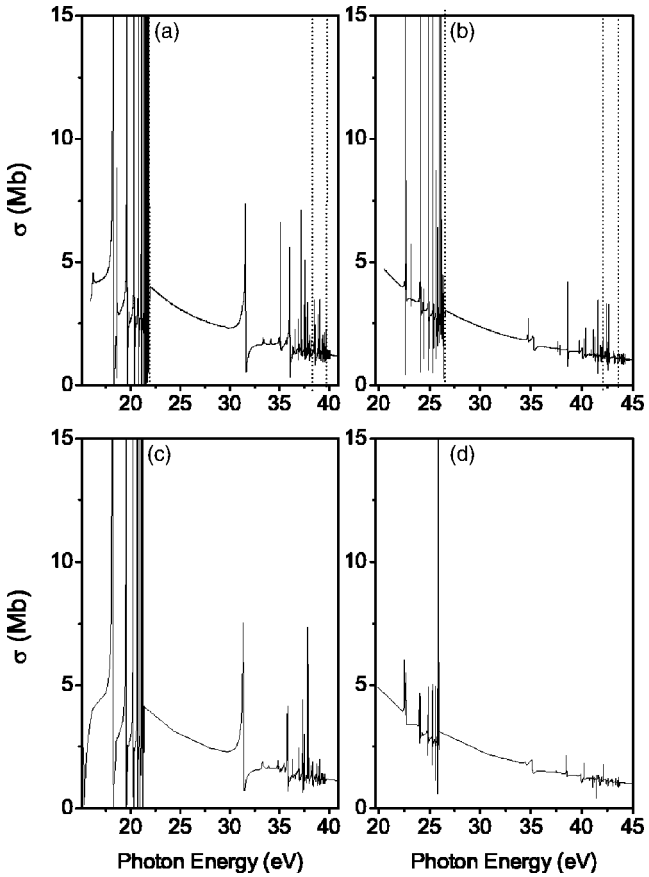

FIG. 5. (a) Total photoionization cross sections for the excited $2s2p\ ^{1,3}P^o$ states of Be-like B^+ ion as a function of photon energy. (a) Present results for $^1P^o$; solid curve, present length; dashed, present velocity. (b) OP results for $^1P^o$. (c) Present results for $^3P^o$; solid curve, present length; dashed, present velocity. (d) OP result for $^3P^o$. The vertical dotted lines represent the B^{2+} $2p$, $3s$, and $3p$ thresholds, respectively.

quite different from present results for both singlet and triplet cases, as shown in Fig. 5. Next, the resonance structure in the OP calculation is slightly shifted to the lower-energy side with respect to our results owing to a slight difference in the threshold energies in the two calculations. Some of the resonances are also rather different, e.g., the OP results do not contain the $3s^2\ ^1S$ resonance at 27.6997 eV which the present calculation finds. Numerous other differences in resonance strengths are seen in the figure, particularly in the ^3P case.

The OP calculation itself [1] differs from the present calculation in two important respects. First, the OP final-state close-coupling expansion contains all states of B^{2+} up to $n=3$, while the present calculation includes up to the $n=4$ states, as discussed in Sec. II. Thus, the present calculation includes a larger basis set, which translates to greater accuracy. Second, the OP calculation treats the full Hamiltonian of the system, but the present calculation deals with the valence-shell Hamiltonian plus an empirical potential to represent the effects of the inner electron, the $1s^2$ shell in this case. As discussed in Sec. II, the empirical potential is chosen to reproduce experimental excitation energies, which makes the energies of the various ionization thresholds much more accurate in the present calculation, as seen in Table II; this, in turn, makes the cross sections resulting from the present calculation significantly more accurate in the region of the various thresholds.

Both ^1P and ^3P total photoionization cross sections are seen to be dominated by Rydberg series of autoionizing resonances converging to the various ionic thresholds. However, the resonances are much stronger in the singlet case, as opposed to the triplet case, as seen in Fig. 5. This could be due to the fact that for the singlet states, the spatial parts of the two-electron wave functions are symmetric, so that the electrons are, on the average, closer together than in the triplet case where the wave functions are antisymmetric. And, in situations where the electrons are closer together, it would be expected that they interact (correlate) more strongly; such an interaction is required to excite the various doubly excited resonances.

IV. CONCLUSIONS

Calculations of partial and total photoionization spectra for the excited $2s2p\ ^{1,3}P$ states of ionic B^+ between the B^{2+} $2s$ and B^{2+} $3d$ thresholds using an eigenchannel R-matrix formalism are presented. These calculations are the most accurate and extensive to date for the photoionization of the first two excited states of ionic B^+. The cross sections in most of the energy regions are dominated by Rydberg series of autoionizing resonances converging to the various ionic thresholds, particularly for the ^1P initial state. While the background (nonresonant) cross sections are similar both qualitatively and quantitatively for the two initial states, the resonances are quite different. This indicates that dynamical effects, effects due to differing intial- and final-state wave functions, in the singlet and triplet channels are of considerable importance.

All of the resonance series up to those converging to the B^{2+} $3d$ state were classified, a nontrivial matter due to the overlapping of the various series in the neighborhood of the $n=3$ thresholds. The untangling of these seemingly chaotic regions would not have been possible without the use of a methodology based on eigenphase sum gradients [14].

To get some idea of the variation of the cross sections along the isoelectronic sequence, it is of interest to compare the results for B^+ with our earlier results for neutral Be [7], especially since exactly the same theoretical methods were employed in both cases. The stronger attractive field of the B^+ moves a number of the strong near-threshold Be resonances below the B^+ ionization threshold, thereby altering the threshold behavior of the cross sections considerably. In addition, the intermixing among the resonances converging to the $2p$ and the various $n=3$ final ionic states is considerably greater for B^+ than for Be, resulting in a much more complex pattern of resonances for B^+ photoionization. This occurs because the energy extent of the resonance series converging to each threshold increases with Z much more rapidly than the splitting of the thresholds; in fact, as $Z\rightarrow\infty$, the $n=3$ thresholds become degenerate. This leads to the implication that the resonance situation becomes even more com-

plex for the photoionization of these excited states of C^{2+} and higher members of the Be isoelectronic sequence. Aside from the above major differences, however, other aspects of the cross sections for both ^1P and ^3P excited initial states are found to be quite similar for Be and B^+.

Agreement with previous calculations is excellent qualitatively and relatively good quantitatively (with some exceptions) for the background cross section and the resonances leading up to the first excited state of B^{2+}. For the higher resonances, there is no previous accurate calculation to compare with, but it is expected that the level of accuracy of the present calculation is no different for these resonances than for the lower ones. Experimental studies would be highly desirable to confirm our understanding of the physics of these photoionization processes.

ACKNOWLEDGMENTS

The authors acknowledge support of this work by Korea Science and Engineering Foundation (Grant No. R05-2004-000-10082-0) in Republic of Korea, NASA, and DOE, Division of Chemical Sciences, Office of Basic Energy Sciences.

[1] J. A. Tully, M. J. Seaton, and K. A. Berrington, J. Phys. B **33**, 3811 (1990).
[2] M. J. Seaton, J. Phys. B **20**, 6363 (1987).
[3] E. Jannitti, F. Pinzhong, and G. Tondello, Phys. Scr. **33**, 434 (1986).
[4] S. Schippers, A. Müller, B. M. McLaughlin, A. Aguilar, C. Cisneros, E. D. Emmons, M. F. Gharaibeh, and R. A. Phaneuf, J. Phys. B **36**, 3371 (2003).
[5] D.-S. Kim and S. T. Manson, J. Phys. B **37**, 4013 (2004).
[6] D.-S. Kim, S. S. Tayal, H.-L. Zhou, and S. T. Manson, Phys. Rev. A **61**, 062701 (2000).
[7] D.-S. Kim, H.-L. Zhou, S. T. Manson, and S. S. Tayal, Phys. Rev. A **64**, 042713 (2001).
[8] F. Robicheaux and C. H. Greene, Phys. Rev. A **46**, 3821 (1992).
[9] F. Robicheaux and C. H. Greene, Phys. Rev. A **46**, 3821 (1992); **47**, 1066 (1993); **48**, 4441 (1993).
[10] P. F. O'Mahony and C. H. Greene, Phys. Rev. A **31**, 250 (1985).
[11] C. H. Greene, Phys. Rev. A **32**, 1880 (1985).
[12] http://physics.nist.gov/cgi-bin/AtData/main_asd
[13] C. H. Greene and Ch. Jungen, Adv. At. Mol. Phys. **21**, 51 (1985).
[14] M. Aymar, C. H. Greene, and E. Luc-Koenig, Rev. Mod. Phys. **68**, 1015 (1996).